

1 | Influence of the sudden stratospheric warming on quasi-2 day  
2 | waves

3 | Sheng-Yang Gu<sup>1,2,3\*</sup>, Han-Li Liu<sup>4</sup>, Xiankang Dou<sup>1,3</sup>, Tao Li<sup>1,3</sup>  
4 |

5 | <sup>1</sup>CAS Key Laboratory of Geospace Environment, Department of Geophysics and  
6 | Planetary Science, University of Science and Technology of China, Hefei, Anhui,  
7 | China

8 | <sup>2</sup>Key Laboratory of Earth and Planetary Physics, Institute of Geology and Geophysics,  
9 | Chinese Academy of Sciences

10 | <sup>3</sup>Mengcheng National Geophysical Observatory, School of Earth and Space Sciences,  
11 | University of Science and Technology of China, Hefei, Anhui, China

12 | <sup>4</sup>High Altitude Observatory, National Center for Atmospheric Research, Boulder,  
13 | Colorado, USA

14 |  
15 |  
16 | \*Corresponding author: S.-Y. Gu, CAS Key Laboratory of Geospace Environment,  
17 | School of Earth and Space Science, University of Science and Technology of China,  
18 | 96 Jin-zhai Rd, Hefei, Anhui 230026, China. (gsy@ustc.edu.cn).

19 **Abstract:**

20 | The influence of the sudden stratospheric warming (SSW) on quasi-2 day wave  
21 (QTDW) with westward zonal wavenumber 3 (W3) is investigated using the  
22 Thermosphere-Ionosphere-Mesosphere-Electrodynamics General Circulation Model  
23 (TIME-GCM). The summer easterly jet below 90 km is strengthened during an SSW,  
24 which results in a larger refractive index and thus more favorable condition for the  
25 propagation of W3. In the winter hemisphere, the Eliassen Palm (EP) flux diagnostics  
26 indicate that the strong instabilities at middle and high latitudes in the mesopause  
27 region are important for the amplification of W3, which are weakened during SSW  
28 periods due to the deceleration or even reversal of the winter westerly winds.  
29 Nonlinear interactions between the W3 and the wavenumber 1 stationary planetary  
30 wave produce QTDW with westward zonal wavenumber 2 (W2). The meridional  
31 wind perturbations of the W2 peak in the equatorial region, while the zonal wind and  
32 temperature components maximize at middle latitudes. The EP flux diagnostics  
33 indicate that the W2 is capable of propagating upward in both winter and summer  
34 hemispheres, whereas the propagation of W3 is mostly confined to the summer  
35 hemisphere. This characteristic is likely due to the fact that the phase speed of W2 is  
36 larger, and therefore its waveguide has a broader latitudinal extension. The larger  
37 phase speed also makes W2 less vulnerable to dissipation and critical layer filtering  
38 by the background wind when propagating upward.

39

40 **1. Introduction**

41 The westward quasi-2 day wave (QTDW) is a predominant phenomenon in the  
42 mesosphere and lower thermosphere (MLT) region in the summer hemisphere with  
43 zonal wavenumbers 2, 3, and 4. The QTDW was observed by the neutral temperature  
44 measurements from Upper Atmosphere Research Satellite (UARS) [Wu *et al.*, 1996],  
45 Aura satellite [Tunbridge *et al.*, 2011] and Thermosphere Ionosphere and Mesosphere  
46 Electric Dynamics (TIMED) satellite [Gu *et al.*, 2013a], and the neutral wind  
47 measurements from UARS High Resolution Doppler Imager (HRDI) [Wu *et al.*, 1993],  
48 TIMED TIDI [Gu *et al.*, 2013a], and medium frequency radar [Gu *et al.*, 2013b]. In  
49 addition, numerical simulations, including one-dimensional model [Plumb, 1983],  
50 two-dimensional model [Rojas and Norton, 2007], three dimensional  
51 Thermosphere-Ionosphere-Mesosphere-Electrodynamics General Circulation Model  
52 (TIME-GCM) [Yue *et al.*, 2012] and the Navy Operational Global Atmospheric  
53 Prediction System Advanced Level Physics, High Altitude (NOGAPS-ALPHA)  
54 forecast-assimilation system [McCormack, 2009], have also been utilized to study the  
55 QTDW. Using neutral temperature and horizontal wind observations from the TIMED  
56 satellite, Gu *et al.* [2013a] showed that the QTDW with westward zonal wavenumber  
57 3 (W3) is amplified during January/February in the southern hemisphere, and that the  
58 QTDW with westward zonal wavenumber 4 (W4) reaches a maximum amplitude  
59 during July/August in the northern hemisphere. The amplitude of the W3 is nearly  
60 twice as strong as the W4. It is proposed that the W3 is the Rossby-gravity mode (3, 0)  
61 [Salby, 1981], which can be modulated by the mean flow instabilities [Plumb, 1983;

62 *Limpasuvan et al.*, 2000; *Salby and Callaghan*, 2001; *Yue et al.*, 2012]. Besides,  
63 *Limpasuvan et al.* [2000] found that the inertial instability in the equatorial region  
64 could also play a role in amplifying QTDW. Nevertheless, the TIME-GCM  
65 experiments performed by *Liu et al.* [2004] showed no clear evidence of QTDW  
66 amplification around inertial unstable regions, which only causes additional spatial  
67 variability. The W4 is first reported by *Rodgers and Prata* [1981] in the radiance data  
68 from the Nimbus 6 satellite, which was also confirmed by *Plumb* [1983] with a  
69 one-dimensional model under summer easterly conditions. Usually, the W4 is  
70 believed to be an unstable mode induced by the summer easterly instabilities [*Plumb,*  
71 1983; *Burks and Leovy*, 1986]. Compared with W3 and W4, there are much less  
72 reports on the QTDW with westward zonal wavenumber 2 (W2).

73 *Tunbridge et al.* [2011] studied the zonal wavenumbers of the summer time  
74 QTDW with satellite temperature observations from 2004 to 2009. They found that  
75 the W2 is amplified mainly during January in the southern hemisphere with a  
76 maximum amplitude at middle latitudes, which always coincides with the temporal  
77 variations of the W3. The horizontal wind observations from the HRDI instrument  
78 onboard the UARS satellite showed that the meridional wind perturbations of the W2  
79 maximize in the equatorial region at the mesopause [*Riggin et al.*, 2004]. This W2  
80 was suggested to be excited in-situ at high altitude, which has little direct connection  
81 with the 2-day activities at lower altitudes. Anomalous 2-day wave activities with  
82 zonal wavenumber 2 were also observed in the Aura/MLS temperature and  
83 line-of-sight wind [*Limpasuvan and Wu*; 2009], which was suggested to be an

84 unstable mode induced by the strong summer easterly jet during January 2006. *Rojas*  
85 *and Norton* [2007] found a wavenumber 2 westward propagating wave mode with a  
86 period of 49 h in a linear two-dimensional model under boreal summer easterly  
87 condition, which maximized at middle and high latitudes in the summer hemisphere  
88 for both temperature and neutral wind components. The zonal wind and meridional  
89 wind perturbations also exhibited a smaller peak at low latitudes in the winter  
90 hemisphere and at the equator, respectively.

91 It is known that nonlinear interactions between planetary scale waves can  
92 contribute to atmospheric variability. For example, [Thermosphere Ionosphere and](#)  
93 [Mesosphere Electric Dynamics \(TIMED\) satellite](#) ~~TIMED/SABER~~ temperature  
94 observations during January 2005 showed that the nonlinear interactions between the  
95 W3 and the migrating diurnal tide could produce an eastward QTDW with zonal  
96 wavenumber 2 [*Palo et al.*, 2007]. The nonlinear interactions between the  
97 quasi-stationary planetary waves (QSPW) and the migrating tides lead to changes in  
98 tides, which then transmit the QSPW signals into the ionosphere at low and middle  
99 latitudes through the E region wind dynamo [*Liu et al.*, 2010; *Liu and Richmond*,  
100 2013]. Nevertheless, the nonlinear interactions between QTDW and other planetary  
101 waves have not been reported.

102 Rapid growth of QSPWs and their forcing are believed to be the main drivers of  
103 the sudden stratospheric warming (SSW) at high latitudes in the winter hemisphere  
104 [*Matsuno*, 1971], which causes inter-hemispheric connections at different altitudes  
105 [e.g. *Karlsson et al.*, 2007, 2009; *Tan et al.*, 2012]. The wave-mean flow interactions

106 | could decelerate or even reverse the eastward winter stratospheric jet, which, in  
107 | return, prevents the further growth of the QSPW. The SSW in the northern  
108 | hemisphere occurs usually in January/February, accompanied with a strong zonal  
109 | wavenumber 1 or 2 QSPW at high latitudes [*Pancheva et al.*, 2008; *Harada et al.*,  
110 | 2009; *Manney et al.*, 2009; *Funke et al.*, 2010]. There have been recent studies  
111 | suggesting possible connection between QTDW and SSW [*McCormick et al.*, 2009;  
112 | *Chandran et al.*, 2013]. However, it is not clear if this is because both QTDW and  
113 | SSW tend to occur in mid to late January, or if the flow condition around SSW is  
114 | more favorable for QTDW propagation and/or amplification. In this paper, we  
115 | investigate the influence of SSW on QTDW using the National Center for  
116 | Atmosphere Research (NCAR) TIME-GCM. The numerical experiments are described  
117 | in section 2. Section 3 are the analysis results from the model simulations. Section 4  
118 | discusses the contributions of QTDW to the summer mesospheric polar warming. Our  
119 | conclusions are presented in section 5.

## 120 | **2. Datasets and analysis**

### 121 | **2.1 TIMED satellite observations**

122 | The ~~Thermosphere-Ionosphere and Mesosphere Electric Dynamics~~ (TIMED)  
123 | satellite was launched at the end of 2001, which focuses on the dynamics study of  
124 | the mesosphere and lower thermosphere. The TIMED Doppler Imager (TIDI)  
125 | instrument on board the TIMED satellite has been providing global horizontal wind  
126 | observations since late January 2002. The NCAR-processed version 0307A of P9 line  
127 | TIDI wind datasets are utilized here to investigate the inter-annual variations of the

128 QTDWs during austral summer periods. The vertical resolution of the TIDI winds  
129 between 85 and 105 km is ~2 km, with the highest precision at ~95 km [*Killeen et al.*,  
130 2006]. The version 0307A TIDI horizontal winds have been used in the study of  
131 mesospheric tidal variations and QTDWs [*Wu et al.*, 2008; *Gu et al.*, 2013]. A  
132 two-dimensional least square fitting method, which was provided by *Gu et al.* [2013a;  
133 2015], is also adopted to extract the QTDW signals in this study.

## 134 **2.2 TIME-GCM simulations**

135 The NCAR TIME-GCM simulates the global atmosphere from the upper  
136 stratosphere to the thermosphere, and the ionospheric electrodynamics [*Roble and*  
137 *Ridley*, 1994; *Roble*, 2000; *Richmond et al.*, 1992], which is self consistent. The input  
138 solar EUV and UV spectral fluxes are parameterized by the solar flux index at 10.7  
139 cm wavelength (F10.7), and it is set to 150 sfu (solar flux unit) in our model  
140 simulations. The auroral electron precipitation is parameterized by hemispheric power  
141 [*Roble and Ridley*, 1987] and the ionospheric convection is driven by the  
142 magnetosphere-ionosphere current system [*Heelis et al.*, 1982]. The hemispheric  
143 power is set to 16 and the cross-cap potential is set to 60 in our simulations. The  
144 gravity wave forcing is parameterized based on linear saturation theory [*Lindzen*,  
145 1981]. Climatologic migrating tides from the Global Scale Wave Model (GSWM) are  
146 specified at the lower boundary. The model is capable of simulating the upward  
147 propagation of planetary waves by superimposing periodical geopotential height  
148 perturbations at the lower boundary (~30 km). We use the regular horizontal  
149 resolution of  $5^{\circ} \times 5^{\circ}$  longitude and latitude grids in the current study. There are 49

150 pressure levels from 10 hPa ( $\sim 30$  km) to the upper boundary of  $3.5 \times 10^{-10}$  hPa ( $\sim 550$   
151 km) with a vertical resolution of one-half scale height. The tides are generally weak  
152 compared with climatology in this single version of TIME-GCM. But this does not  
153 alter our conclusion with regard to 2-day waves.

154 To simulate the QTDW, geopotential height perturbations of 1000 m with  
155 wavenumber 3 were forced at the TIME-GCM lower boundary. The Gaussian-shaped  
156 geopotential height perturbations for W3 peaked at  $30^\circ \text{N}$ , extending from  $10^\circ \text{S}$  to  
157  $70^\circ \text{N}$ . To simulate the SSW, geopotential height perturbations of 1000 and 2800 m for  
158 a stationary planetary wave with zonal wavenumber 1 (SPW1) were specified at the  
159 lower boundary for weak and strong warming, respectively. The Gaussian-shaped  
160 geopotential height perturbations for SPW1 peaked at  $60^\circ \text{N}$ , extending from  $35^\circ \text{N}$  to  
161  $85^\circ \text{N}$ . In fact, the European Centre for Medium-Range Weather Forecasts (ECMWF)  
162 dataset during 2011/2012 austral summer period shows that both the geopotential  
163 perturbations of the W3 and SPW1 maximize in the northern (winter) hemisphere at  
164 the model lower boundary (not shown). The model was run under perpetual  
165 conditions for 40 days with the calendar date set to January 20. Both the W3 and  
166 SPW1 gained maximum amplitudes on day 10 with a Gaussian-shaped increase from  
167 day 1 to 10. The forcing of W3 was reduced following the same Gaussian function  
168 from days 25 to 40. The forcing of SPW1 was sustained from days 10 to 40. The  
169 parameters for the control run (base case) and four different experimental runs (case 1,  
170 2, 3, and 4) are summarized in Table 1. No W3 or SPW1 forcing was specified at the  
171 TIME-GCM lower boundary in the base case, which ran for 15 days to equilibrate and

172 was utilized as initial conditions for the other experimental cases. Case 1 was a  
173 standard run for W3 and only geopotential height perturbations of W3 were forced.  
174 Case 2 and case 3 were designed to study the amplification of W3 under weak and  
175 strong SSW conditions, respectively. The same W3 forcing was added in cases 2 and  
176 3, whereas the SPW1 forcing was stronger in case 3 than that in case 2. Case 4 was a  
177 standard run for SSW in which only the forcing of SPW1 was included.

### 178 **3. Observational results**

179 Figure 1 shows the ECMWF zonal mean temperature at 80N and 10 hPa from  
180 December to February during 2003-2012. The strongest SSW occurred in January  
181 2009, followed by the second strongest SSW in January 2006. Besides, the SSWs in  
182 2012, 2004 and 2010 were also very strong. Figure 2 shows the temporal variations of  
183 the wave number 3 QTDW in January and February during 2003-2012. The  
184 amplitudes were averaged between 90 and 100 km. The W3 peaked regularly in late  
185 January and early February every year but with strong inter-annual variabilities. For  
186 example, the W3 reached minima in January of 2008 and 2009. It is also clear that the  
187 W3 was strong during the strong SSW years of 2004, 2006 and 2012. Nevertheless,  
188 the W3 was extremely weak during the strongest SSW year of 2009. Figure 3 shows  
189 the averaged amplitudes of the wave number 2 QTDW between 90 and 100 km during  
190 2003-2012, which also maximized in January and February. The W2 was the strongest  
191 during the strong SSW year of 2006, followed by the W2 event in 2012. We can see  
192 that the QTDWs could be very strong during some SSW years, but not during all the  
193 SSW years. Our question is whether the SSW and QTDW (both W2 and W3) impact

194 each other, and this will be numerically studied in the following section.

## 195 **4. Simulation results and Discussion**

### 196 **4.1 Zonal mean background condition**

197 Since the model time was set perpetually on January 20, the background  
198 temperature and zonal wind in our simulations should show typical northern  
199 winter/southern summer conditions. Figures 4a and 4b show the zonal mean  
200 temperature and zonal mean zonal wind on model day 28 (when W3 peaks) in case 1,  
201 which only has W3 forcing. The zonal mean temperature in TIME-GCM shows a cold  
202 summer mesopause and a warm winter mesopause. In the upper stratosphere and  
203 mesosphere, the zonal mean zonal wind is easterly~~westward~~ in the summer  
204 ~~hemisphere~~mesosphere and westerly~~eastward~~ in the winter ~~hemisphere~~mesosphere. It  
205 is clear that the global structures of the zonal mean temperature and zonal wind  
206 generally agree with climatology from for example previous TIMED/SABER  
207 temperature [*Mertens et al.*, 2009] and UARS/HRDI wind [*Swinbank and Ortland*,  
208 2003] observations, as well as the NOGAPS-ALPHA forecast assimilations  
209 [*McCormack*, 2009].

210 We then investigate the atmospheric responses to the weak and strong SSW event  
211 in cases 2 and 3, respectively. Figures 4c and 4e show the temperature differences on  
212 model day 28 between case 2 and case 1, and between case 3 and case 1, respectively.  
213 In cases 1, 2 and 3, the same W3 forcing is specified at the lower boundary, whereas  
214 SPW1 is only specified in cases 2 and 3. The SPW1 forcing in case 2 is weaker than  
215 that in case 3. Compared with case 1, which does not have a stationary planetary wave

216 specified at the model lower boundary, the temperature of case 2 is warmer by 15-20  
217 K below 60 km and is colder by 20-25 K between 60 and 110 km at high latitudes in  
218 the winter hemisphere. Both the cooling and warming in case 3 are stronger than in  
219 case 2 due to the stronger SPW1 in case 3. The warming and cooling in the  
220 stratosphere and mesosphere for the strong SSW are ~40 K and ~60 K, respectively.  
221 In addition, weaker warming is observed between 70 and 100 km in the middle and  
222 low latitude regions and above 80 km at high latitudes in the summer hemisphere. The  
223 corresponding zonal mean zonal wind differences are shown in Figure 4d and 4f. The  
224 zonal mean zonal wind decreases by ~30 m/s and ~70 m/s in the winter stratosphere  
225 and lower mesosphere in the weak (case 2) and strong (case 3) SSW events,  
226 respectively. It increases by ~30 m/s and ~50 m/s in the mesopause region in the weak  
227 and strong SSW events, respectively. Generally, the SSW features in our simulations  
228 (e.g. the increasing temperature and decreasing westerly in the winter stratosphere  
229 high latitude region) agree with previous reports [Funke *et al.*, 2010; Yamashita *et al.*,  
230 2010; Tan *et al.*, 2012].

## 231 **4.2 The influences on W3**

232 Figure 5a shows the wavenumber-period spectrum of the meridional wind during  
233 days 25-30 of case 1. The meridional wind at ~~~82~~90 km and ~~722~~722.5 °S is utilized in the  
234 analysis. The westward wavenumber 3 QTDW dominates the whole spectrum, with  
235 negligible signatures at other wavenumbers and periods. The spectra of zonal wind  
236 and temperature show similar W3 signatures as the meridional wind (not shown).  
237 Figure 5b shows the latitudinal and vertical structure of the W3 in meridional wind,

238 which maximizes at low latitudes in the southern hemisphere mesopause region with  
239 an amplitude of ~60 m/s. Shown in Figure 5c is the structure of the W3 in zonal wind,  
240 which peaks at middle and low latitudes in both hemispheres with maximum  
241 amplitude nearly half of the peak meridional wind amplitude. The zonal wind peak of  
242 ~30 m/s in the summer (southern) hemisphere is slightly larger than that of ~20 m/s in  
243 the winter hemisphere, most likely due to the additional amplification by the  
244 baroclinic/barotropic instability of the summer easterly. Figure 5d shows the global  
245 structure of the W3 in temperature, which also peaks at middle latitudes. In the  
246 summer hemisphere, the temperature perturbations peak at ~105 km and ~80 km with  
247 amplitudes of ~7 K and ~8 K, respectively. In the winter hemisphere, the peak of the  
248 W3 at ~80 km is much weaker than that between 100 and 110 km. We should note  
249 that the rapid decay of W3 near the model lower boundary (~30 km) is an artifact near  
250 the model lower boundary. In all, the vertical and latitudinal structures of the 2-day  
251 wave in our simulations generally agree with the TIMED/SABER temperature and  
252 TIMED/TIDI observations [*Palo et al.*, 2007; *Gu et al.*, 2013].

253 | Figure 6 shows the temporal variations of the W3 in meridional wind at ~9082  
254 km for case 1, case 2 and case 3. Note that the same perturbations for W3 were forced  
255 at the lower model boundary for all the three experimental runs. The W3 forcing was  
256 gradually increased from day 1 to 10, and was reduced after day 25 with constant  
257 amplitude between day 10 and 25. The perturbations of SPW1 in case 2 were nearly  
258 three times larger than case 3, both of which were sustained after day 10 with a  
259 Gaussian-shaped increase from day 1 to 10. The W3 in case 1 is the strongest with an

260 amplitude of ~60 m/s (Figure 6a). The maximum amplitudes of the W3 in case 2 and  
 261 case 3 are ~40 m/s and ~35 m/s (Figure 6b and 6c), respectively. It is evident that the  
 262 amplitudes of the W3 are weakened during the SSW periods. In the following, we will  
 263 examine possible causes of the QTDW decrease during SSW.

264 The refractive index  $m$  of a forced planetary wave is [Andrews *et al.*, 1987]:

$$265 \quad m^2 = \frac{\bar{q}_\varphi}{a(\bar{u} - c)} - \frac{s^2}{(ac \circ \wp)^2} - \frac{f^2}{4N^2H^2}, \quad (1)$$

266 where  $s$ ,  $c$ ,  $\bar{u}$ ,  $a$ ,  $\varphi$ ,  $f$ ,  $N$ , and  $H$  are the zonal wavenumber, phase speed, zonal mean  
 267 zonal wind, earth radius, latitude, Coriolis parameter, Brunt-Väisälä frequency, and  
 268 scale height, respectively. Besides,  $\bar{q}_\varphi$  is the latitudinal gradient of the  
 269 quasi-geostrophic potential vorticity:

$$270 \quad \bar{q}_\varphi = 2\Omega c \circ \wp - \left( \frac{\bar{u}c \circ \wp}{ac \circ \wp} \right)_\varphi - \frac{a}{\rho} \left( \frac{f^2}{N^2} \rho \bar{u}_z \right)_z, \quad (2)$$

271 where  $\Omega$  is the angular speed of the earth's rotation,  $\rho$  is the background air density,  
 272 and  $z$  means the vertical gradient. A necessary condition for baroclinic/barotropic  
 273 instability is  $\bar{q}_\varphi < 0$ , and the planetary waves are propagating (evanescent) where  $m^2$   
 274 is positive (negative). Moreover, the meridional and vertical components (EPY and  
 275 EPZ) of the Eliassen-Palm (EP) flux vector ( $\vec{F}$ ) for planetary waves can also be  
 276 calculated with reconstructed wave perturbations from the TIME-GCM, defined  
 277 following Andrews *et al.* [1987] as:

$$278 \quad \vec{F}_{EP} = \begin{bmatrix} \text{EPY} \\ \text{EPZ} \end{bmatrix} = \rho a \cos \varphi \begin{bmatrix} \frac{\overline{u_z v' \theta'}}{\theta_z} - \overline{v' u'} \\ \left[ f - \frac{(\bar{u} \cos \varphi)_\varphi}{a \cos \varphi} \right] \frac{\overline{v' \theta'}}{\theta_z} - \overline{w' u'} \end{bmatrix} \quad (3)$$

279 Here  $u'$ ,  $v'$ ,  $w'$  and  $\theta'$  are the QTDW perturbations in zonal wind,  
280 meridional wind, vertical wind and potential temperature, respectively.

281 First, we examine the baroclinic/barotropic instabilities, waveguide and the EP  
282 flux of the W3 for these cases. The averaged zonal mean zonal wind for case 1, case 2  
283 and case 3 during days 25-30, when the W3 reaches the maximum amplitude, are  
284 depicted by the black contour lines in Figures 7a, 7c and 7e, respectively.  
285 Over-plotted are the negative regions of  $\bar{q}_\phi$  by blue shades, which is a prerequisite for  
286 the occurrence of mean flow instability, and the positive regions of the waveguide for  
287 W3 by orange shades, which show where wave propagation is favorable. Shown in  
288 Figures 7b, 7d and 7f are the EP flux vectors (red arrows) of W3 and their divergences  
289 (light blue shades and dot lines) for case 1, case 2 and case 3, respectively. We will  
290 first compare results of case 1 (Figures 7a and 7b) with case 2 (Figures 7c and 7d). A  
291 region of negative  $\bar{q}_\phi$  is seen in case 1 between 80 and 100 km at middle and high  
292 latitudes in the winter hemisphere, which are insignificant in case 2. This difference  
293 probably results from the different vertical shears in zonal wind between the two  
294 cases. Moreover, the region with negative  $\bar{q}_\phi$  in the summer stratosphere polar region  
295 is also slightly more ~~expansive~~~~extended~~ in case 1. Correspondingly, the positive EP  
296 flux divergence for W3, which is an indication of wave source, is stronger in both the  
297 summer mesosphere polar region and the winter mesopause region for case 1. The  
298 positive EP flux divergence near the polar region of summer mesosphere is suggested  
299 to be evidence of wave amplification from the baroclinic/barotropic unstable region  
300 [Liu *et al.*, 2004]. The additional source for the W3 is evident from the positive EP

301 flux divergence atby the southward edge of the baroclinic/barotropic instability in the  
302 winter mesopause region for case 1 (Figure 7b).

303 Case 1 (Figures 7a and 7b) and case 3 (Figures 7e and 7f) are now compared.  
304 The stratospheric westerlies in the winter hemisphere polar region reverse to easterlies  
305 in case 3, which creates an area with negative  $\bar{q}_\phi$  in the winter polar mesosphere and  
306 stratopause, compared with case 1 (Figures 7a and 7e). Previous studies have found  
307 that planetary waves could be generated by the anomalous potential vorticity  
308 gradients in the winter middle atmosphere [Zülicke and Becker, 2013; Sato and  
309 Nomoto, 2015]. During SSW periods, the planetary wave signals are clearly indicated  
310 by the outflow of the EP flux vectors and positive EP flux divergences nearby the  
311 baroclinic/barotropic instabilities induced by the reversal of winter westerly  
312 [Limpasuvan et al., 2012; Chandran et al., 2013]. In our simulations, ~~T~~the additional  
313 W3 sources between 60°N and 90°N below 70 km in case 3 may be related to the  
314 nearby instability (Figures 7b and 7f), as found by Liu et al. [2004]. It is also seen that  
315 the summer easterly winds in case 3 are stronger than in case 2 and case 1, which  
316 results in a larger refractive index for the propagation of W3. The EP flux vectors in  
317 all the experimental runs show that the W3 propagates mainly southward from the  
318 northern hemisphere wave source region at lower altitudes, and then propagates  
319 upward after reaching the southern hemisphere. These propagation features agree well  
320 with previous model simulations [Chang et al., 2011; Yue et al., 2012].

321 The meridional and vertical components of the W3 EP flux (EPY and EPZ) are  
322 shown in Figure 8. It is clear that both the EPY and EPZ are the strongest in case 1,

323 which is probably due to the energy transfer to child waves during the nonlinear  
324 interaction between W3 and SPW1 for cases 2 and 3. In the northern (winter)  
325 hemisphere, the stronger EPY and EPZ in case 1 may also be induced by the  
326 | additional northern mesospheric barotropic/baroclinic instabilities (shown in Figure  
327 7a), which is not found in case 2 and case 3. The EPY components for all three cases  
328 indicate southward propagation at lower altitudes from the wave source region in the  
329 winter hemisphere, and then northward propagation in the summer polar mesosphere  
330 near the region of instability. The EPZ mostly propagates upward, and is the strongest  
331 at middle and low latitudes in the summer hemisphere and much weaker in the winter  
332 hemisphere. This is in general agreement with the waveguide shown in Figure 7.  
333 Strong upward EPZ at ~30°N and ~100 km is only observed in case 1, which is  
334 probably related to the instability at middle and high latitudes (Figure 7a). Such  
335 instabilities and wave sources disappear in the SSW runs due to the deceleration or  
336 even reversal of the strong winter westerly winds.

337 Our simulations show that the instabilities at middle and high latitudes in the  
338 winter hemisphere mesopause region can also provide additional and significant  
339 sources for the amplification of W3 (case 1). Such instabilities and the corresponding  
340 sources for W3 are weakened during SSW periods due to the deceleration or even  
341 reversal of the winter stratospheric westerly winds. Our results also show that the  
342 summer easterlies in the stratosphere and lower mesosphere are strengthened during  
343 SSW periods, which results in larger waveguide and thus more favorable background  
344 condition for the propagation of W3. The fact that W3 becomes weaker in the

345 presence of more favorable propagation conditions (and with the same wave source)  
346 in the summer hemisphere again suggests a loss of W3 wave energy. In the following  
347 section, we argue that the wave energy is transferred to child waves from nonlinear  
348 interaction of W3 with SPW1, namely the QTDW W2 component.

### 349 **4.3 Nonlinear interaction between W3 and SPW1**

350 Figure 9a shows the wavenumber-period spectrum of the meridional wind during  
351 model days 15-20 in case 3 at 100 km and 2.5 °N. A westward wavenumber 2 QTDW  
352 dominates the spectrum, which is different from the wavenumber 3 QTDW signature  
353 shown in Figure 5a. The spectra of other components, e.g., zonal wind and  
354 temperature, also show evident wavenumber 2 QTDW signatures. We should  
355 emphasize that W3 and SPW1 are the only planetary waves specified at the lower  
356 boundary of the TIME-GCM and no W2 signals are detected in the TIME-GCM runs  
357 with only W3 or SPW1 perturbations imposed at the lower boundary (case 1 and case  
358 4). Thus, the W2 in case 2 and case 3 is generated by the nonlinear interaction  
359 between W3 and SPW1. The nonlinear interactions between two planetary waves can  
360 generate two child waves with frequencies and zonal wavenumbers being the sum and  
361 difference of the two parent waves [*Teitelbaum and Vial, 1991*]. For the nonlinear  
362 interactions between W3 and SPW1, the frequencies ( $f$ , cycles per day) and zonal  
363 wavenumbers ( $s$ ) of the parents waves are:  $(f, s) = (0.5, 3)$  and  $(0, 1)$ . Note here  
364 positive (negative)  $s$  indicates a westward (eastward) propagating wave. Thus the  
365 child waves are:  $(f, s) = (0.5, 4)$  and  $(0.5, 2)$ . However, the wavenumber 4 QTDW is  
366 not well resolved in our simulation due to its lower phase speed and larger dissipation

367 rate.

368 Figure 9b shows the cross section of the W2 in meridional wind for case 3 during  
369 model days 15-20. It maximizes in the equatorial and low latitude regions at ~100 km  
370 with a maximum amplitude of ~50 m/s. Shown in Figure 9c is the structure of the W2  
371 in zonal wind and it peaks at middle latitudes with an amplitude nearly half as strong  
372 as the meridional wind. Figure 9d shows the global structure of the W2 in temperature,  
373 which exhibits similar global distributions as zonal wind. The temperature  
374 perturbations show maximum amplitudes of ~10 K in both hemispheres at ~105 km,  
375 and secondary maxima at ~85km: ~7 K in the southern hemisphere and ~5 K in the  
376 northern hemisphere. Figures 10a and 10b show the temporal variations of the W2 in  
377 meridional wind at 100 km for case 2 and case 3, respectively. The perturbations of  
378 the W2 in case 2 are weaker than in case 3, with maximum meridional wind  
379 amplitudes of ~35 m/s and ~55 m/s, respectively. This increase in the W2 amplitude  
380 in case 3 is consistent with the nonlinear interaction mechanism since one of the  
381 parent waves (SPW1) is stronger in case 3, resulting in a stronger child wave.

382 The mean flow instabilities, the waveguide and the EP flux of W2 are also  
383 examined to study the wave propagation and amplification. Figures 11a and 11c show  
384 the zonal mean zonal wind during model days 15-20, when the W2 reaches the  
385 strongest amplitude, for case 2 and case 3, respectively. In the northern hemisphere of  
386 case 3, the winter westerly in the upper stratosphere and lower mesosphere  
387 mesospheric winter westerlies in case 3 are reversed in the polar region (Figure 11c),  
388 resulting in strong-weak instabilities in this region. Weak instabilities are also

389 observed at high latitudes in the winter mesopause region for case 2. In the southern  
390 hemisphere, the summer easterly jet core at middle latitudes is stronger in case 3,  
391 which results in a larger waveguide and thus more favorable condition for the  
392 propagation of W2 [Liu *et al.*, 2004]. The mean flow instabilities in the summer polar  
393 region are similar between case 2 and case 3.

394 Figures 11b and 11d show the EP flux of W2 and its divergence for case 2 and  
395 case 3, respectively. The EP flux vectors show that W2 propagates in both summer  
396 and winter hemispheres with comparable strength, which accounts for the nearly  
397 symmetric global distribution of the wave perturbations (Figure 9). The propagation  
398 features of W2 are different from W3 on that the W3 is more favorable to propagate in  
399 the summer hemisphere (Figure 7). This is mainly due to the relatively larger phase  
400 speed of W2, which results in a wider latitudinal distribution of positive waveguide  
401 for W2 and makes W2 less vulnerable to dissipation and critical layer filtering when  
402 propagating upward in the winter hemisphere [Salby and Callaghan, 2001]. Positive  
403 EP flux divergence is seen between 60 and 80 km at middle and high latitudes of the  
404 summer hemisphere for both case 2 and case 3, which is probably due to the wave  
405 amplification by the nearby region of instability [Liu *et al.*, 2004]. In addition, large  
406 positive EP flux divergence regions are found at middle and high latitudes of the  
407 northern hemisphere between 50-100 km for both case 2 and case 3, which is an  
408 indication of wave source due to the nonlinear interaction between SPW1 and W3. In  
409 addition, the positive EP flux divergence of W3 between 30°N and 60°N below 80 km  
410 (Figure 11d) may be related to the negative  $\bar{q}_\phi$  in the winter polar stratosphere (Figure

411 | 11c). This also agrees with the SSW-generating planetary wave signals presented by  
 412 | previous studies [Liu et al., 2004; Limpasuvan et al., 2012; Chandran et al., 2013].

413 | Figure 12 shows the meridional and vertical components (EPY and EPZ) of the EP  
 414 | flux of W2 separately. Both the EPY and EPZ are stronger in case 3 than case 2,  
 415 | which is again consistent with the nonlinear interaction mechanism. The vertical  
 416 | component EPZ (Figures 12b and 12d) clearly shows that the W2 propagates upward  
 417 | nearly symmetrically in both summer and winter hemispheres.

418 |       Figures 13a and 13b show the EP fluxes of W3 and SPW1 during model days  
 419 | 15-20 in case 3. Strong upward propagating SPW1 from wave source region is seen at  
 420 | middle and high latitudes in the winter hemisphere. Meanwhile, the energy of W3  
 421 | propagates mainly southward from the same wave source region. Thus the nonlinear  
 422 | coupling between SPW1 and W3 is most likely to occur at lower altitudes in the  
 423 | winter hemisphere near the wave source region. In addition, weaker W3 energy can  
 424 | also be identified at higher altitudes and at middle and low latitudes in the winter  
 425 | hemisphere, which, together with the strong-SPW1 energyactivities at the same region,  
 426 | could also contribute to the source of W2 through nonlinear coupling. These  
 427 | speculations are further investigated by calculating the nonlinear advectiononve  
 428 | tendency between W3 and SPW1. The nonlinear advectiononve tendency terms in the  
 429 | momentum equations, which have been utilized by *Chang et al.* [2011] in studying the  
 430 | nonlinear coupling between QTDW and tides, are of the form:

$$431 \quad \vec{F}_{advection} = -\vec{V} \cdot \nabla \vec{V} = -\left\{ \frac{u}{a \cos \varphi} \frac{\partial}{\partial \lambda} + \frac{v}{a} \frac{\partial}{\partial \varphi} + w \frac{\partial}{\partial z} \right\} \begin{bmatrix} u \\ v \end{bmatrix}^T \quad (4)$$

432 | Where  $u$ ,  $v$  and  $w$  are the zonal, meridional and vertical winds,  $a$ ,  $z$ ,  $\varphi$  and  $\lambda$  are the

433 earth radius, altitude, latitude, and longitude. By decomposing wind components,  
 434 including zonal, meridional and vertical winds, into the forms of  $r \approx \bar{r} + r_1 + r_2$  ( $\bar{r}$ ,  $r_1$   
 435 and  $r_2$  represent the zonal mean wind and the wind perturbations of the two planetary  
 436 waves, respectively), the zonal and meridional components of the nonlinear coupling  
 437 tendencies for two planetary waves are:

$$438 \quad \bar{F}_{nonlinear,x} = \frac{1}{a \cos \varphi} (u_1 \frac{\partial u_2}{\partial \lambda} + u_2 \frac{\partial u_1}{\partial \lambda}) - \frac{1}{a} (v_1 \frac{\partial u_2}{\partial \varphi} + v_2 \frac{\partial u_1}{\partial \varphi}) - (w_1 \frac{\partial u_2}{\partial z} + w_2 \frac{\partial u_1}{\partial z})$$

439 ~~(5)~~

$$440 \quad F_{nonlinear} = -\frac{1}{a \cos \varphi} (u_1 \frac{\partial v_2}{\partial \lambda} + u_2 \frac{\partial v_1}{\partial \lambda}) - \frac{1}{a} (v_1 \frac{\partial v_2}{\partial \varphi} + v_2 \frac{\partial v_1}{\partial \varphi}) - (w_1 \frac{\partial v_2}{\partial z} + w_2 \frac{\partial v_1}{\partial z})$$

441 ~~\_\_\_\_\_ (6)~~

442 where  $\bar{u}$ ,  $\bar{v}$  and  $\bar{w}$  are the zonal mean zonal, meridional and vertical winds,  $u_1$   
 443 and  $u_2$ ,  $v_1$  and  $v_2$ ,  $w_1$  and  $w_2$  are the zonal, meridional, vertical wind perturbations for  
 444 two different planetary waves. ~~By adopting a complex perturbation of the form~~  
 445  ~~$u' = \hat{u} e^{i(\sigma t - s\lambda)}$  (the  $\sigma$  and  $s$  are the frequency and zonal wavenumber of the planetary~~  
 446 ~~wave,  $t$  is the universal time), the complex amplitudes of the nonlinear advective~~  
 447 ~~tendencies can be calculated as:~~

$$448 \quad \bar{F}_{nonlinear,x} = \frac{i\hat{u}_1\hat{u}_2}{a \cos \varphi} (s_1 + s_2) - \frac{1}{a} (\hat{v}_1 \frac{\partial \hat{u}_2}{\partial \varphi} + \hat{v}_2 \frac{\partial \hat{u}_1}{\partial \varphi}) - (\hat{w}_1 \frac{\partial \hat{u}_2}{\partial z} + \hat{w}_2 \frac{\partial \hat{u}_1}{\partial z}) \quad (7)$$

$$449 \quad \bar{F}_{nonlinear,y} = \frac{i}{a \cos \varphi} (\hat{u}_1\hat{v}_2s_2 + \hat{u}_2\hat{v}_1s_1) - \frac{1}{a} (\hat{v}_1 \frac{\partial \hat{v}_2}{\partial \varphi} + \hat{v}_2 \frac{\partial \hat{v}_1}{\partial \varphi}) - (\hat{w}_1 \frac{\partial \hat{v}_2}{\partial z} + \hat{w}_2 \frac{\partial \hat{v}_1}{\partial z}) \quad (8)$$

450 ~~where  $s_1$  and  $s_2$  are the zonal wavenumbers of different planetary waves,  $\hat{u}_1$~~   
 451 ~~and  $\hat{u}_2$ ,  $\hat{v}_1$  and  $\hat{v}_2$ ,  $\hat{w}_1$  and  $\hat{w}_2$  are the zonal, meridional, vertical wind~~  
 452 ~~amplitudes for two different planetary waves.~~

453 Figure 13c shows the amplitude of the meridional component of the nonlinear  
454 advection~~onve~~ tendency between W3 and SPW1 (equation 85). The nonlinear coupling  
455 between W3 and SPW1 maximizes at lower altitudes in the northern hemisphere,  
456 which is not surprising since both the W3 and SPW1 perturbations are forced at the  
457 lower model boundary in the northern hemisphere. Correspondingly, a strong W2  
458 source is present at lower altitudes in the northern hemisphere, which is also  
459 suggested by the positive EP flux divergence shown in Figure 11d. The large  
460 nonlinear advection value at the lower boundary is due to the large wave sources  
461 forced there to compensate for the unrealistic wave decay usually found near the  
462 model lower boundary. Although the amplitude of the advection~~onve~~ tendency at the  
463 lower model boundary may be too large compared with the peak in the mesosphere, it  
464 is still likely that the nonlinear interaction between W3 and SPW1 at ~~~10 hPa~~30-45  
465 km in the winter hemisphere is strong, since climatologically the sources of W3 and  
466 SPW1 are found to maximize in the winter hemisphere at stratospheric heights. There  
467 is an additional region extending from 60 km to about 100 km at low to mid latitudes  
468 where the advection~~onve~~ tendency term becomes significant (with a peak at ~70km).  
469 This is again consistent with the positive EP flux divergence in Figure 11d, and is  
470 likely due to the nonlinear coupling of W3 and SPW1.

## 471 5. Conclusions

472 The influence of the SSW on the QTDW was investigated with NCAR  
473 TIME-GCM simulations. The westward wavenumber 3 QTDW was simulated by  
474 specifying geopotential height perturbations of 1000 m at the lower model boundary

475 (~30 km) for both the standard W3 run and the SSW runs. Wavenumber 1 stationary  
476 planetary waves with geopotential height perturbations of 1000 m and 2800 m were  
477 forced in the northern hemisphere at the lower model boundary to induce minor and  
478 major SSWs, respectively.

479 We find that the mean flow instabilities at middle and high latitudes in the winter  
480 mesopause region can provide additional and essential sources for the amplification of  
481 W3, whereas such instabilities are weakened during SSW periods due to the  
482 deceleration or even reversal of the winter westerlies. The mean flow instabilities in  
483 the winter stratosphere polar region, induced by the mean wind reversal from westerly  
484 to easterly during SSW periods may also contribute to the amplification of W3. The  
485 waveguide of the W3 is larger during SSW periods, which favors the propagation of  
486 W3. The wave energy of W3 could be transmitted to child waves through the  
487 nonlinear interaction between W3 and stationary planetary waves during the SSW  
488 periods.

489 The nonlinear interaction between W3 and the SPW1 results in a new kind of  
490 westward QTDW with zonal wavenumber 2. The W2 is generated mainly in the wave  
491 source region, and then propagates into both summer and winter hemispheres. The  
492 meridional wind perturbations of W2 maximize in the equatorial region, whereas the  
493 zonal wind and temperature components peak at middle latitudes. The EP flux  
494 diagnostics show that W2 is capable of propagating in both hemispheres, which  
495 results in much more symmetric global structures than W3 for both wind and  
496 temperature components. This is probably due to the larger phase speed of W2, which

497 results in larger latitudinal distributions of positive waveguide and makes W2 less  
498 vulnerable to dissipation and critical layer filtering by the background wind when  
499 propagating upward. In the summer hemisphere, the instabilities in the upper  
500 stratosphere and lower mesosphere polar region may contribute to the amplification of  
501 W2 through wave-mean flow interaction. In the winter hemisphere, the nonlinear  
502 coupling between W3 and SPW1 at middle and low latitudes between 50 km and 100  
503 km, and the instabilities induced by the reversal of winter stratospheric westerly  
504 during SSW periods, most probably provide additional sources for W2. The stronger  
505 stationary planetary wave accounts for the stronger W2 perturbations during major  
506 SSW period by transmitting more energy to W2 during the nonlinear interaction  
507 between W3 and SPW1. Moreover, the background mean flow condition is also more  
508 favorable for the propagation of W2 during major SSW period with a larger  
509 waveguide.

510 We should note that the amplitudes of W3 and SPW1 specified at the lower  
511 boundary were both set to constant values in our simulation, while the wave sources  
512 would vary with time in real atmosphere. In addition, we utilized climatological state  
513 in January as the background condition in the simulation, which may be slightly  
514 different from the mean wind during specific years. For example, the SSWs generated  
515 in our simulation can only be classified as minor ones. Moreover, the TIMED  
516 observations (Figures 2 and 3) show that the W3 is usually much stronger than W2,  
517 even during strong SSW years of 2006 and 2009. Nevertheless, the W2 is even  
518 stronger than W3 in case 3. That is because the SPW1 forcing specified at the

519 TIME-GCM lower boundary is stronger than observation to compensate the  
520 unrealistic wave dissipation at the lower boundary, which result in much stronger  
521 child wave of W2 during the nonlinear interaction. We also note that the W2 and W3  
522 are both much stronger during the 2006 polar vortex displacement SSW event, but  
523 they are very weak during the 2009 vortex split SSW event. The different influence of  
524 the two types of SSW on QTDW also deserves our further investigation. In the future,  
525 the Whole Atmosphere Community Climate Model will be utilized~~we plan to use~~  
526 ~~more realistic assimilation datasets (e.g., ECMWF) as the lower model boundary to~~  
527 further study the influence of SSW on QTDWs under realistic atmospheric conditions,  
528 which may show new light onto~~to understand~~ the variability of the ~~wave~~  
529 ~~sources,~~QTDW and their possible ~~relation~~correlations with SSW.

530

### 531 **Acknowledgements**

532 This work is funded by the Project Supported by the Specialized Research Fund  
533 for State Key Laboratories, the Project Funded by China Postdoctoral Science  
534 Foundation, the National Natural Science Foundation of China (41274150, 41421063),  
535 the Chinese Academy of Sciences Key Research Program (KZZD-EW-01-1), the  
536 National Basic Research Program of China (2012CB825605). HLL. acknowledges  
537 support from NSF grant AGS-1138784. The data utilized in this paper is from  
538 TIME-GCM simulations on NCAR Yellowstone computing system  
539 (ark:/85065/d7wd3xhc). The National Center for Atmospheric Research is sponsored  
540 by the National Science Foundation.

541 **Reference**

542 Andrews, D. G., J. R. Holton, and C. B. Leovy (1987), Middle Atmosphere Dynamics,  
543 489 pp., Academic, San Diego, Calif.

544 Burks, D., and C. Leovy (1986), Planetary waves near the mesospheric easterly jet,  
545 *Geophys. Res. Lett.*, *13*, 193-196, doi: 10.1029/GL013i003p00193.

546 Chandran, A., R. R. Garcia, R. L. Collins, and L. C. Chang (2013), Secondary  
547 planetary waves in the middle and upper atmosphere following the stratospheric  
548 sudden warming event of January 2012, *Geophys. Res. Lett.*, *40*, 1861–1867,  
549 doi:10.1002/grl.50373.

550 Chang, L. C., S. E. Palo, and H. L. Liu (2011), Short-term variability in the migrating  
551 diurnal tide caused by interactions with the quasi 2 day wave, *J. Geophys. Res.*,  
552 *116*, D12112, doi:10.1029/2010JD014996.

553 Funke, B., M. López-Puertas, D. Bermejo-Pantaleón, M. García-Comas, G. P. Stiller,  
554 T. von Clarmann, M. Kiefer, and A. Linden (2010), Evidence for dynamical  
555 coupling from the lower atmosphere to the thermosphere during a major  
556 stratospheric warming, *Geophys. Res. Lett.*, *37*, L13803,  
557 doi:10.1029/2010GL043619.

558 Gu, S. Y., T. Li, X. K. Dou, Q. Wu, M. G. Mlynczak, and J. M. Russell (2013a),  
559 Observations of Quasi-Two-Day wave by TIMED/SABER and TIMED/TIDI, *J.*  
560 *Geophys. Res. Atmos.*, *118*, 1624–1639, doi:10.1002/jgrd.50191.

561 Gu, S. Y., T. Li, X. Dou, N.-N. Wang, D. Riggin, and D. Fritts (2013b), Long-term  
562 observations of the quasi two-day wave by Hawaii MF radar, *J. Geophys. Res.*

563 *Space Physics*, 118, 7886–7894, doi:10.1002/2013JA018858.

564 Harada, Y., A. Goto, H. Hasegawa, N. Fujikawa, H. Naoe, and T. Hirooka (2009), A  
565 Major Stratospheric Sudden Warming Event in January 2009, *J. Atmos. Sci.*, 67,  
566 2052-2069, doi:http://dx.doi.org/10.1175/2009JAS3320.1.

567 Heelis, R. A., J. K. Lowell, and R. W. Spiro (1982), A model of the high-latitude  
568 ionsphere convection pattern, *J. Geophys. Res.*, 87, 6339–6345.

569 Karlsson, B., H. Körnich, and J. Gumbel (2007), Evidence for interhemispheric  
570 stratosphere-mesosphere coupling derived from noctilucent cloud properties,  
571 *Geophys. Res. Lett.*, 34, L16806, doi:10.1029/2007GL030282.

572 Karlsson, B., C. McLandress, and T. G. Shepherd (2009), Inter-hemispheric  
573 mesospheric coupling in a comprehensive middle atmosphere model, *J. Atmos.*  
574 *Sol. Terr. Phys.*, 71, 518-530, doi:10.1016/j.jastp.2008.08.006.

575 Limpasuvan, V., and D. L. Wu (2009), Anomalous two-day wave behavior during the  
576 2006 austral summer, *Geophys. Res. Lett.*, 36, L04807,  
577 doi:10.1029/2008GL036387.

578 Limpasuvan, V., C. B. Leovy, and Y. J. Orsolini (2000), Observed temperature  
579 two-day wave and its relatives near the stratopause, *J. Atmos. Sci.*, 57, 1689-1701,  
580 doi:10.1175/1520-0469(2000)057%3C1689:OTTDWA%3E2.0.CO;2.

581 Limpasuvan, V., J. H. Richter, Y. J. Orsolini, F. Stordal, and O.-K. Kvissel (2012), The  
582 roles of planetary and gravity waves during a major stratospheric sudden  
583 warming as characterized in WACCM, *Journal of Atmospheric and*  
584 *Solar-Terrestrial Physics*, 78–79, 84-98.

585 Lindzen, R. S. (1981), Turbulence and Stress Owing to Gravity Wave and Tidal  
586 Breakdown, *J. Geophys. Res.*, *86*, 9707-9714, doi:10.1029/JC086iC10p09707.

587 Liu, H. L., E. R. Talaat, R. G. Roble, R. S. Lieberman, D. M. Riggin, and J. H. Yee  
588 (2004), The 6.5-day wave and its seasonal variability in the middle and upper  
589 atmosphere, *J. Geophys. Res.*, *109*, D21112, doi:10.1029/2004JD004795.

590 Liu, H. L., and A. D. Richmond (2013), Attribution of ionospheric vertical plasma  
591 drift perturbations to large-scale waves and the dependence on solar activity, *J.*  
592 *Geophys. Res.*, *118*, 2452-2465, doi:10.1002/jgra.50265.

593 Liu, H. L., W. Wang, A. D. Richmond, and R. G. Roble (2010), Ionospheric variability  
594 due to planetary waves and tides for solar minimum conditions, *J. Geophys. Res.*,  
595 *115*, A00G01, doi:10.1029/2009JA015188.

596 Manney, G. L., et al. (2009), Satellite observations and modeling of transport in the  
597 upper troposphere through the lower mesosphere during the 2006 major  
598 stratospheric sudden warming, *Atmos Chem Phys*, *9*, 4775-4795,  
599 doi:10.5194/acp-9-4775-2009.

600 Matsuno, T. (1971), A Dynamical Model of the Stratospheric Sudden Warming, *J.*  
601 *Atmos. Sci.*, *28*, 1479-1494,  
602 doi:http://dx.doi.org/10.1175/1520-0469(1971)028<1479:ADMOTS>2.0.CO;2.

603 McCormack, J. P., L. Coy, and K. W. Hoppel (2009), Evolution of the quasi 2-day  
604 wave during January 2006, *J. Geophys. Res.*, *114*, D20115,  
605 doi:10.1029/2009JD012239.

606 Mertens, C. J., et al. (2009), Kinetic temperature and carbon dioxide from broadband

607 infrared limb emission measurements taken from the TIMED/SABER instrument,  
608 *Adv. Space. Res.*, *43*, 15-27.

609 Palo, S. E., J. M. Forbes, X. Zhang, J. M. Russell, III, and M. G. Mlynczak (2007), An  
610 eastward propagating two-day wave: Evidence for nonlinear planetary wave and  
611 tidal coupling in the mesosphere and lower thermosphere, *Geophys. Res. Lett.*,  
612 *34*, L07807, doi:10.1029/2006GL027728.

613 Pancheva, D., et al. (2008), Latitudinal wave coupling of the stratosphere and  
614 mesosphere during the major stratospheric warming in 2003/2004, *Ann.*  
615 *Geophys.*, *26*, 467-483, doi:10.5194/angeo-26-467-2008.

616 Plumb, R. A. (1983), Baroclinic Instability of the Summer Mesosphere: A Mechanism  
617 for the Quasi-Two-Day Wave?, *J. Atmos. Sci.*, *40*(1), 262-270,  
618 doi:10.1175/1520-0469(1983)040<0262:BIOTSM>2.0.CO;2.

619 Richmond, A. D., E. C. Ridley, and R. G. Roble (1992), A thermosphere/ionosphere  
620 general circulation model with coupled electrodynamics, *Geophys. Res. Lett.*, *19*,  
621 601–604.

622 Riggin, D. M., R. S. Lieberman, R. A. Vincent, A. H. Manson, C. E. Meek, T.  
623 Nakamura, T. Tsuda, and Y. I. Portnyagin (2004), The 2-day wave during the  
624 boreal summer of 1994, *J. Geophys. Res.*, *109*, D08110,  
625 doi:10.1029/2003JD004493.

626 Roble, R. G. (2000), On the feasibility of developing a global atmospheric model  
627 extending from the ground to the exosphere, in *Atmospheric Science Across the*  
628 *Stratopause*, edited by D. E. Siskind, S. D. Eckermann, and M. E. Summers, 342

629 p., no. 123 in Geophysical Monograph Series, American Geophysical Union,  
630 Washington, D.C.

631 Roble, R. G., and E. C. Ridley (1987), An auroral model for the NCAR thermosphere  
632 general circulation model (TGCM), *Annales. Geophysicae.*, 5A, 369–382.

633 Roble, R. G., and E. C. Ridley (1994), A  
634 thermosphere-ionosphere-mesosphere-electrodynamics general circulation model  
635 (time-GCM): Equinox solar cycle minimum simulations (30–500 km), *Geophys.*  
636 *Res. Lett.*, 21, 417-420, doi:10.1029/93GL03391.

637 Rodgers, C. D., and A. J. Prata (1981), Evidence for a Traveling 2-Day Wave in the  
638 Middle Atmosphere, *J Geophys Res.*, 86, 9661-9664,  
639 doi:10.1029/JC086iC10p09661.

640 Rojas, M., and W. Norton (2007), Amplification of the 2-day wave from mutual  
641 interaction of global Rossby-gravity and local modes in the summer mesosphere,  
642 *J. Geophys. Res.*, 112, D12114, doi:10.1029/2006JD008084.

643 Salby, M. L. (1981), The 2-Day Wave in the Middle Atmosphere: Observations and  
644 Theory, *J. Geophys. Res.*, 86, 9654-9660, doi:10.1029/JC086iC10p09654.

645 Salby, M. L., and P. F. Callaghan (2001), Seasonal Amplification of the 2-Day Wave:  
646 Relationship between Normal Mode and Instability, *J. Atmos. Sci.*, 58(14),  
647 1858-1869,  
648 doi:10.1175/1520-0469(2001)058%3C1858:SAOTDW%3E2.0.CO;2.

649 [Sato, K., and M. Nomoto \(2015\), Gravity Wave–Induced Anomalous Potential](#)  
650 [Vorticity Gradient Generating Planetary Waves in the Winter Mesosphere,](#)

651 | [Journal of the Atmospheric Sciences, 72\(9\), 3609-3624.](#)

652 Swinbank, R., and D. A. Ortland (2003), Compilation of wind data for the Upper  
653 Atmosphere Research Satellite (UARS) Reference Atmosphere Project, *J.*  
654 *Geophys. Res.*, *108*, 4615.

655 Tan, B., X. Chu, H.-L. Liu, C. Yamashita, and J. M. Russell, III (2012), Zonal-mean  
656 global teleconnection from 15 to 110 km derived from SABER and WACCM, *J.*  
657 *Geophys. Res.*, *117*, D10106, doi:10.1029/2011JD016750.

658 Teitelbaum, H., and F. Vial (1991), On Tidal Variability Induced by  
659 Nonlinear-Interaction with Planetary-Waves, *J Geophys Res.*, *96*, 14169-14178,  
660 doi:10.1029/91JA01019.

661 Tunbridge, V. M., D. J. Sandford, and N. J. Mitchell (2011), Zonal wave numbers of  
662 the summertime 2 day planetary wave observed in the mesosphere by EOS Aura  
663 Microwave Limb Sounder, *J. Geophys. Res.*, *116*, D11103,  
664 doi:10.1029/2010jd014567.

665 Wu, D. L., E. F. Fishbein, W. G. Read, and J. W. Waters (1996), Excitation and  
666 Evolution of the Quasi-2-Day Wave Observed in UARS/MLS Temperature  
667 Measurements, *Journal of the Atmospheric Sciences*, *53*, 728-738,  
668 doi:10.1175/1520-0469(1996)053<0728:EAEOTQ>2.0.CO;2.

669 Wu, D. L., P. B. Hays, W. R. Skinner, A. R. Marshall, M. D. Burrage, R. S. Lieberman,  
670 and D. A. Ortland (1993), Observations of the Quasi 2-Day Wave from the  
671 High-Resolution Doppler Imager on Uars, *Geophys. Res. Lett.*, *20*, 2853-2856,  
672 doi:10.1029/93GL03008.

673 Yamashita, C., H. -L. Liu, and X. Chu (2010), Responses of mesosphere and lower  
674 thermosphere temperatures to gravity wave forcing during stratospheric sudden  
675 warming, *Geophys. Res. Lett.*, 37, L09803, doi:10.1029/2009GL042351.

676 Yue, J., H.-L. Liu, and L. C. Chang (2012), Numerical investigation of the quasi 2 day  
677 wave in the mesosphere and lower thermosphere, *J. Geophys. Res.*, 117, D05111,  
678 doi:10.1029/2011JD016574.

679 Zülicke, C., and E. Becker (2013), The structure of the mesosphere during sudden  
680 stratospheric warmings in a global circulation model, *Journal of Geophysical*  
681 *Research: Atmospheres*, 118(5), 2255-2271.

682

683

	GP Height of W3	GP Height of SPW1
Base case	×	×
Case 1	1000 m	×
Case 2	1000 m	1000 m
Case 3	1000 m	2800 m
Case 4	×	2800 m

684

**Table 1.** The geopotential height perturbations of W3 and SPW1 specified at the lower model boundary for different model runs.

685

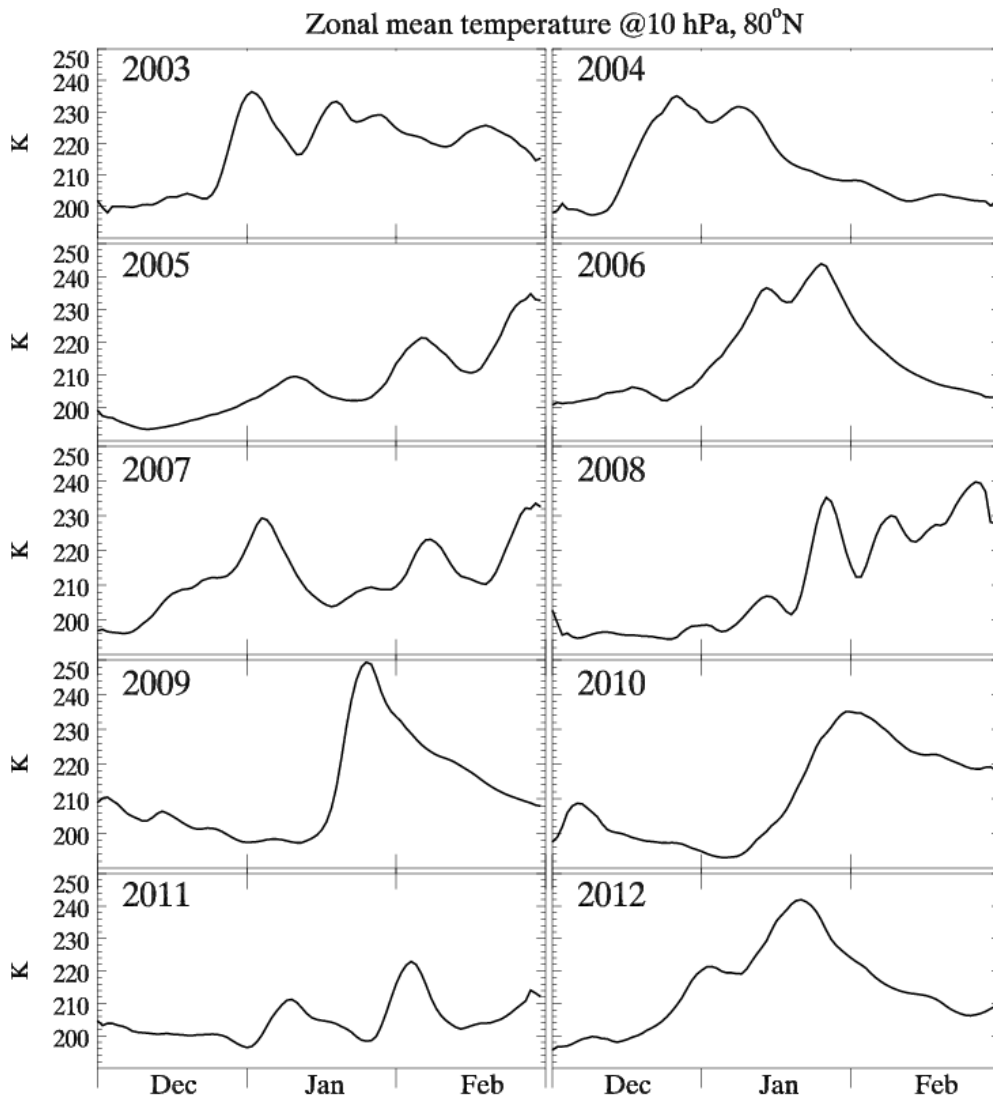
686

687

688

689

690



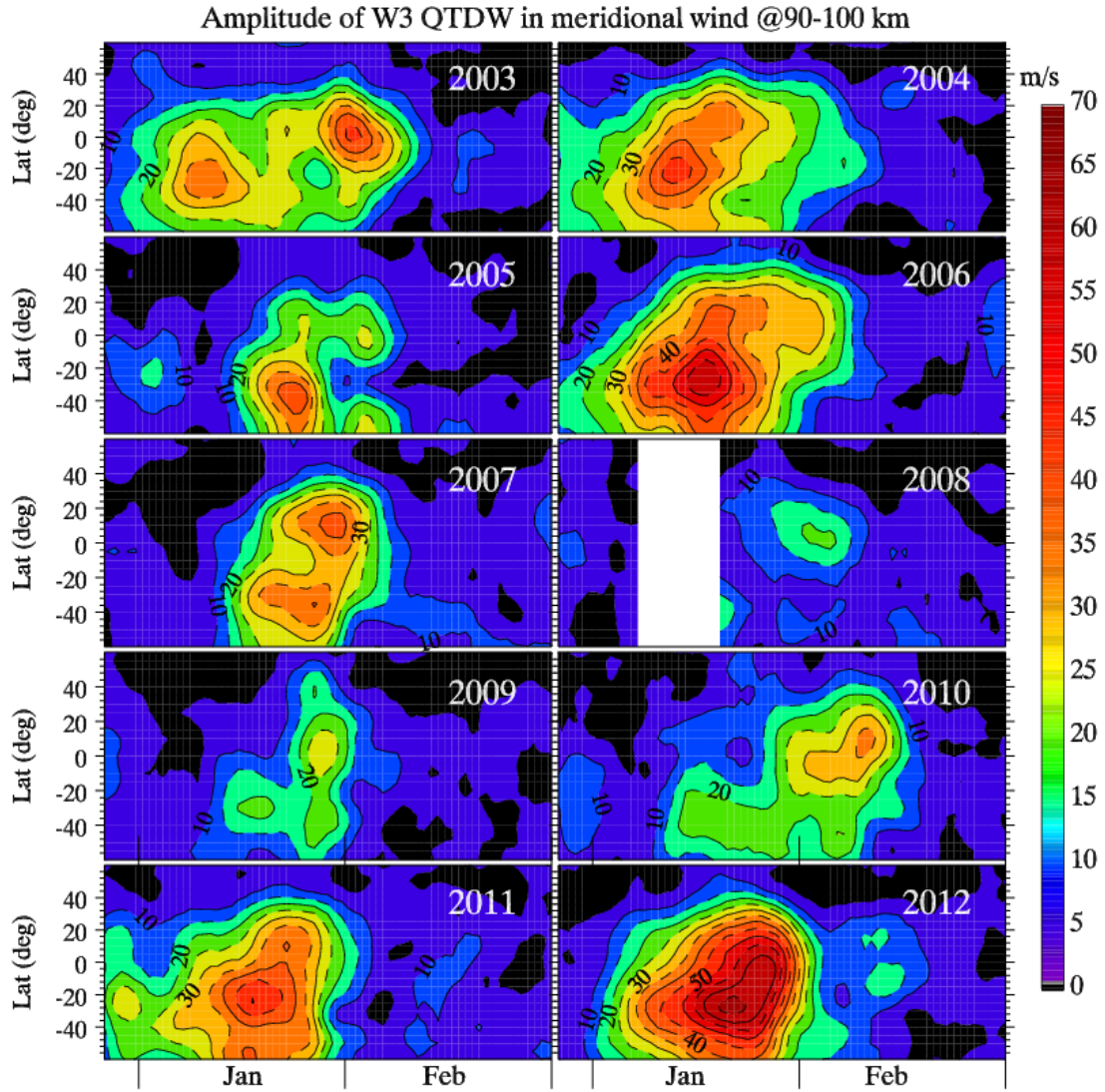
692

693

694

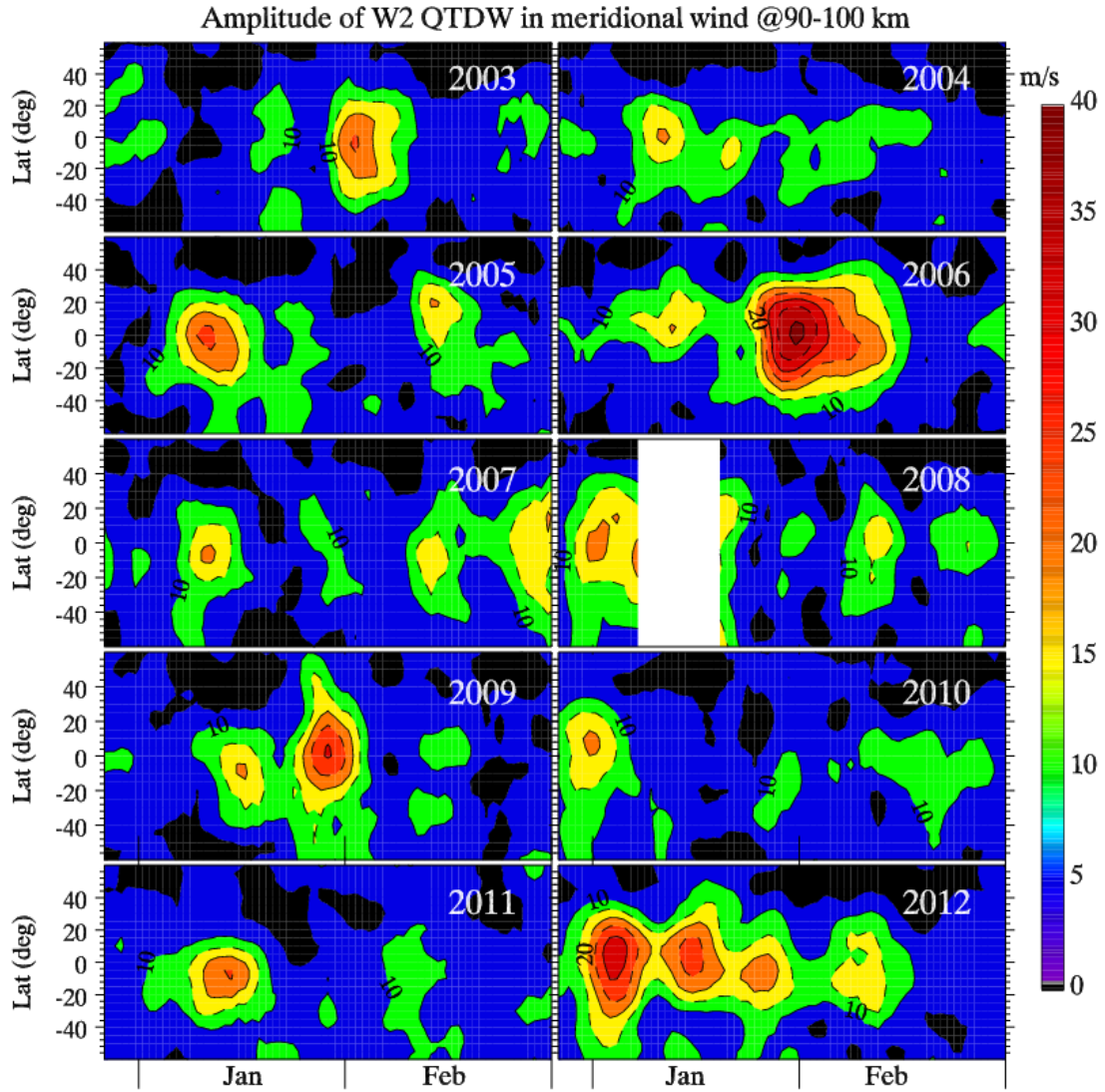
695

Figure 1. The ECMWF zonal mean temperature at 80 °N and 10 hPa from December to February during 2003-2012.



696  
 697  
 698  
 699

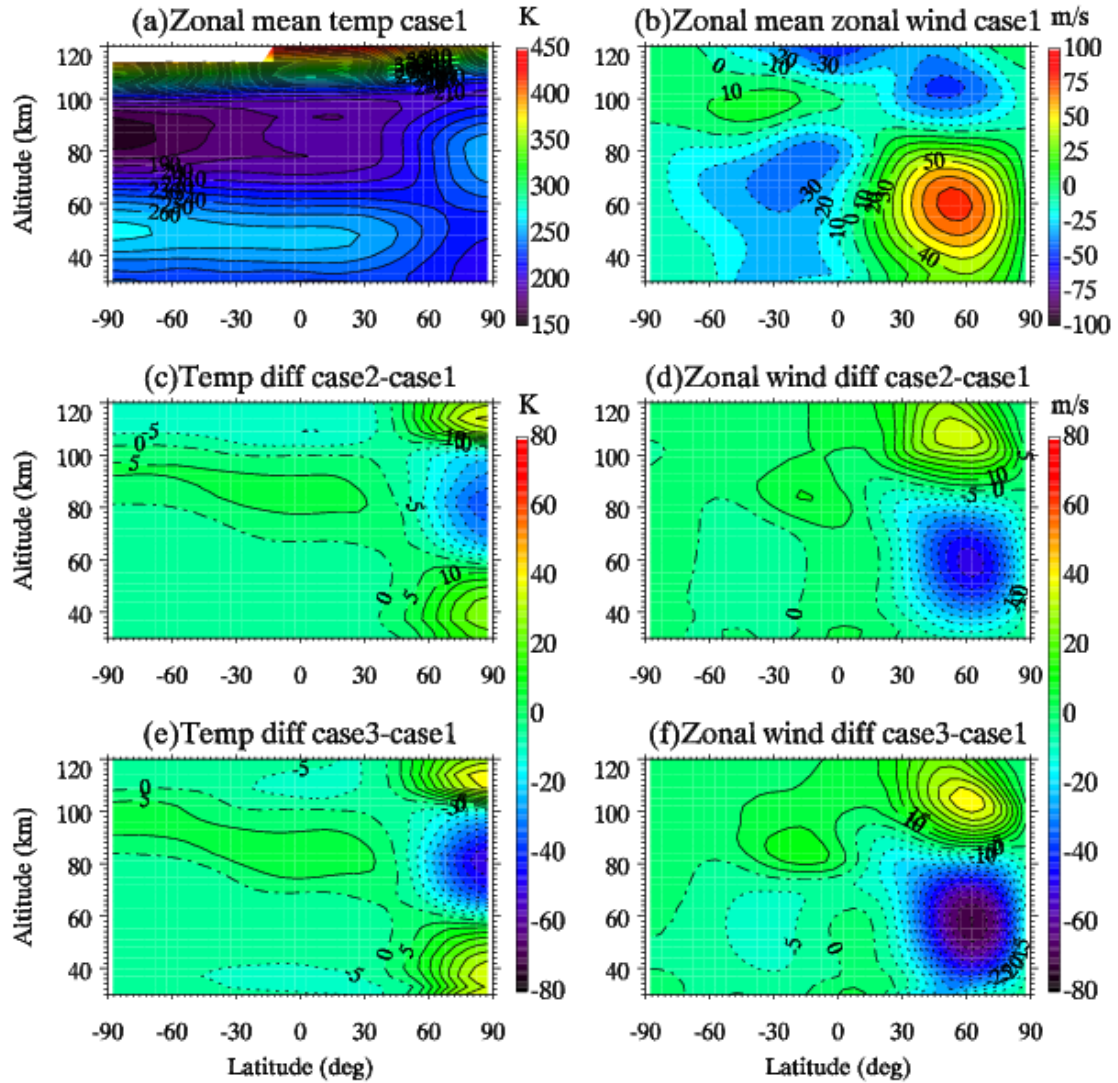
Figure 2. The temporal variations of the wave number 3 QTDW in January and February during 2003-2012. The amplitudes are averaged between 90 and 100 km.



700

701

Figure 3. The same as Figure 2 but for the wave number 2 QTDW.



702

703

704 **Figure 4.** The zonal mean (a) temperature and (b) zonal wind in case 1 on model day

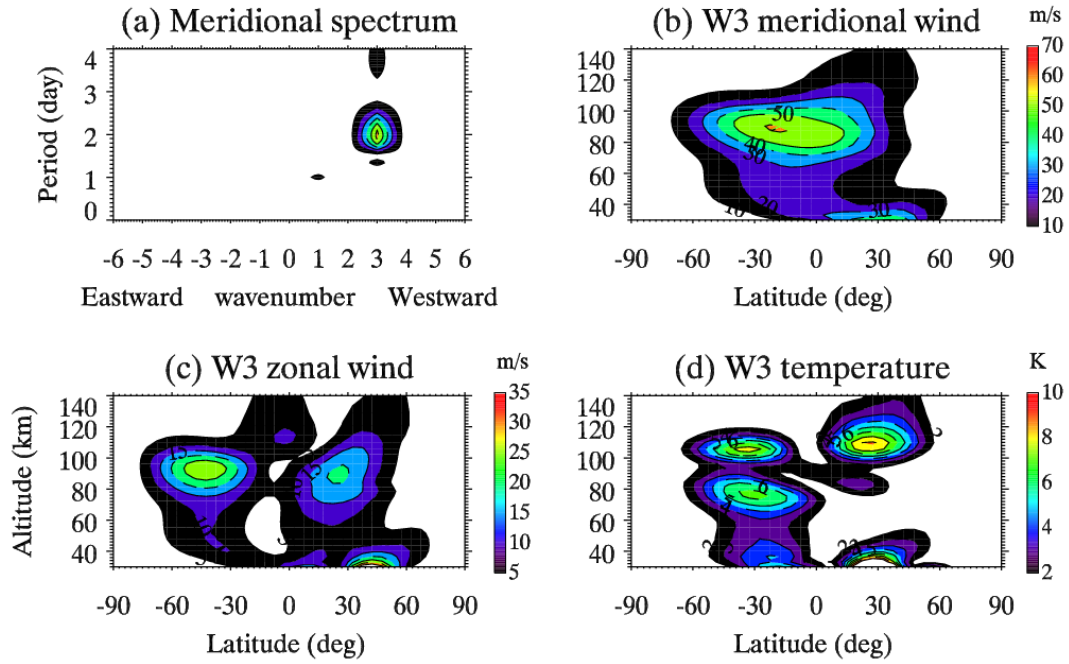
705

706 case 3 and case 1 are also shown. The temperature contour intervals are 10 K in (a)

707

708

(d) and (f).

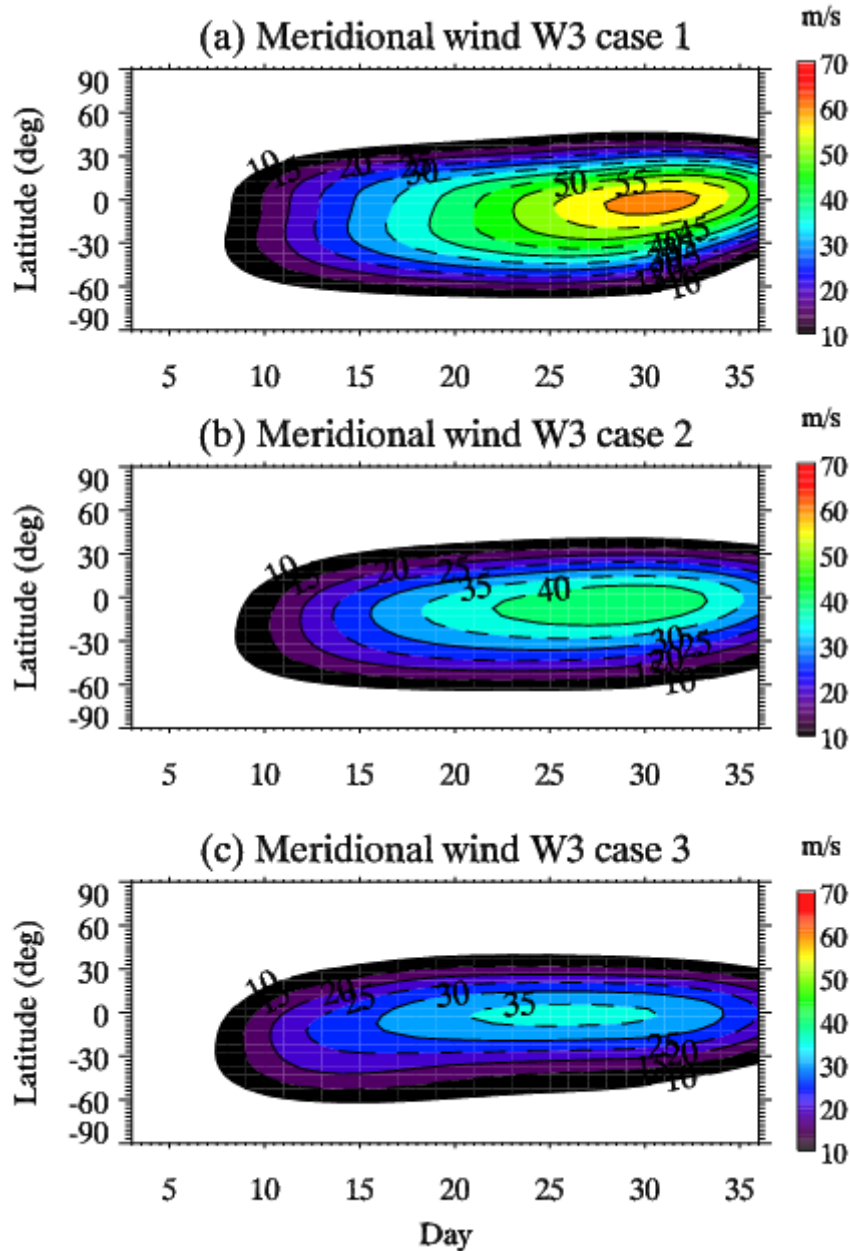


709

710 **Figure 5.** (a) The least-square fitting spectrum of the meridional wind at 22.5°S and  
 711 ~90 km during model day 25-30 of case 1. A westward wave number 3 QTDW  
 712 dominates the spectrum. The vertical and global structures of the W3 in meridional  
 713 wind, zonal wind and temperature are shown in (b), (c) and (d), respectively. The  
 714 contour intervals are 10 m/s, 5 m/s and 1 K for meridional wind, zonal wind and  
 715 temperature, respectively.

716

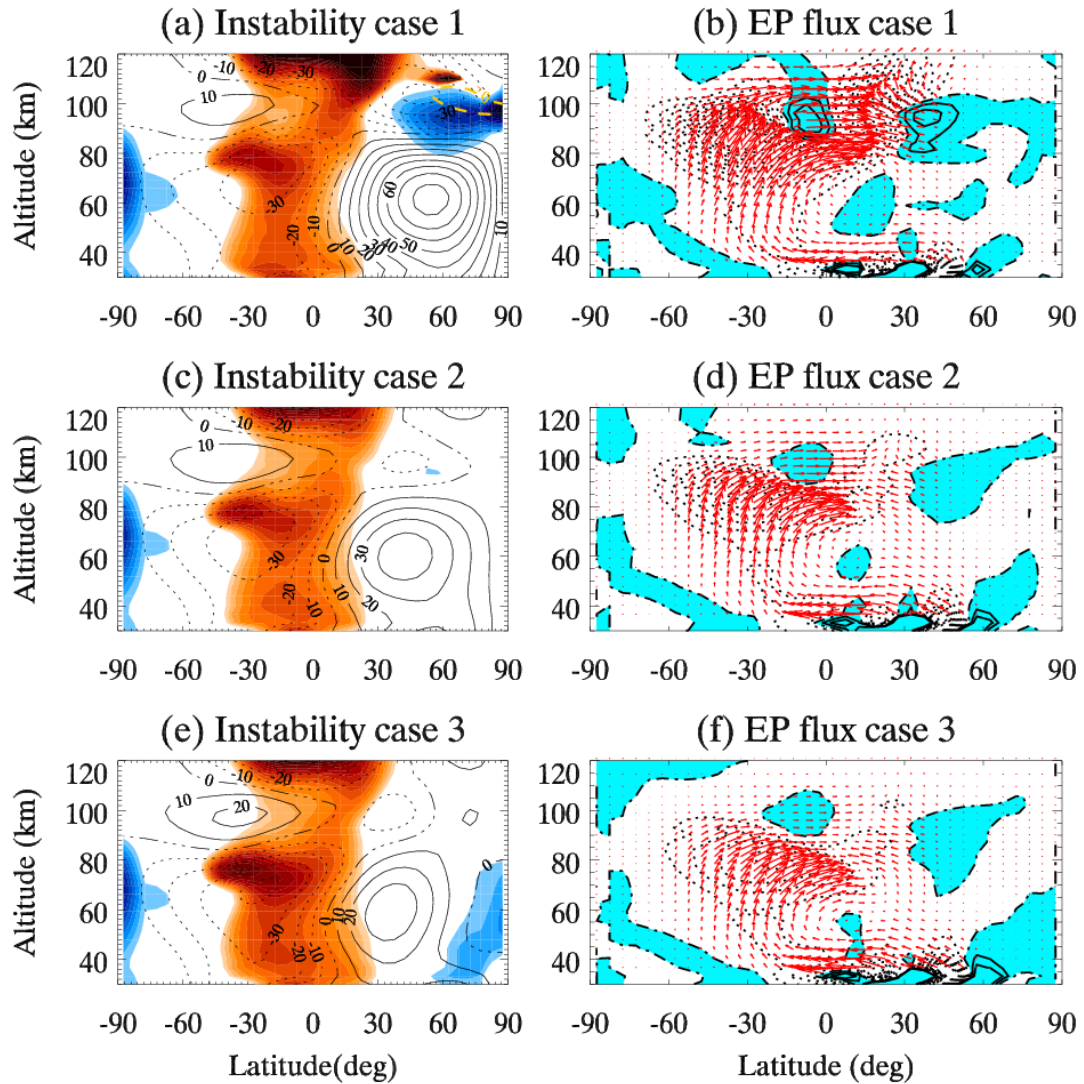
717



718

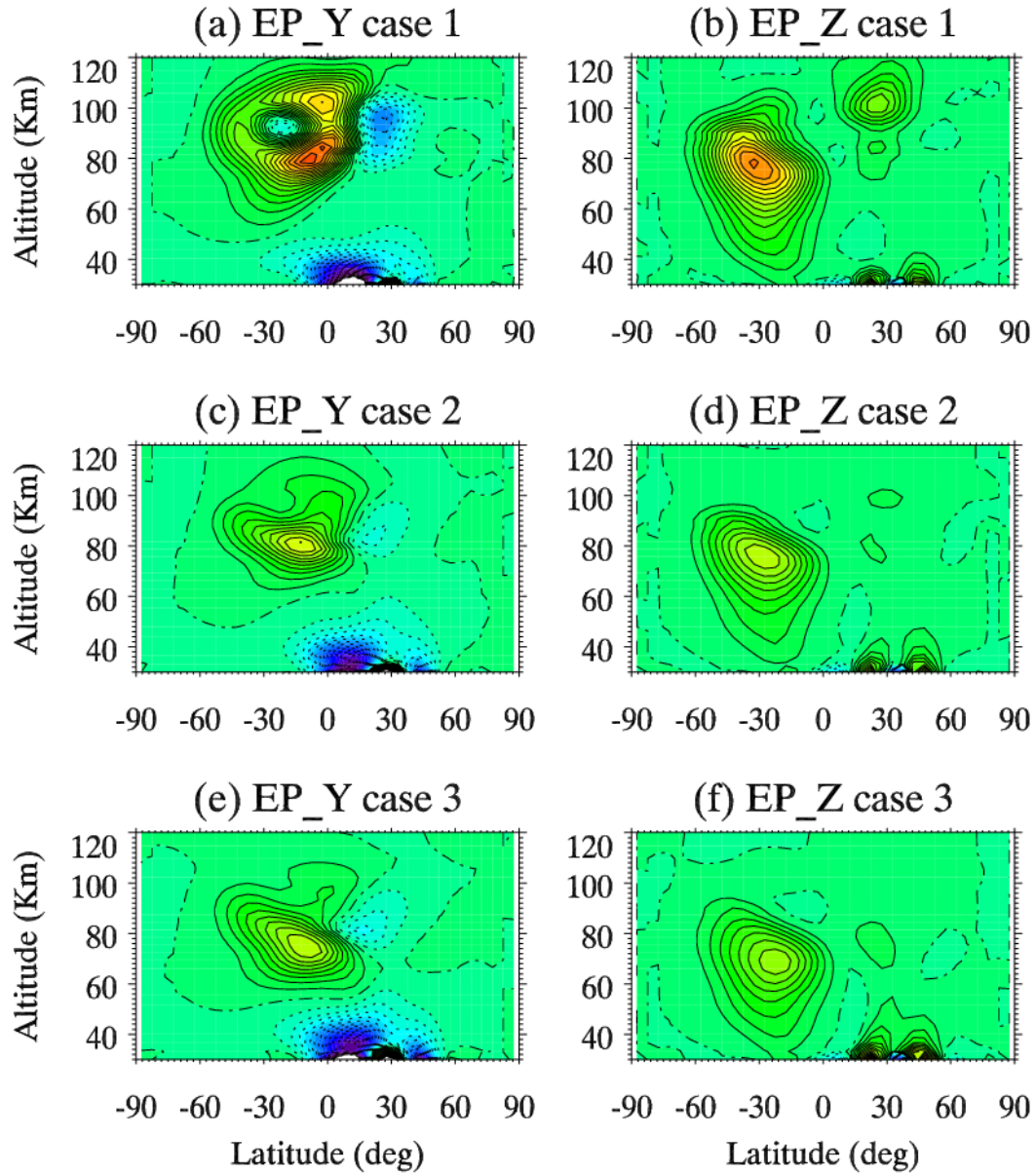
719 | **Figure 6.** The temporal variations of the W3 at 9082 km for (a) case 1, (b) case 2 and  
 720 (c) case 3. Geopotential height perturbations of 1000 m are forced at the lower  
 721 boundary for all the three control runs to simulate the W3. SPW1 geopotential height  
 722 perturbations of 1000 m and 2800 m are forced at the lower boundary to induce the  
 723 weak and strong SSWs in case 2 and case 3, respectively. No SPW1 perturbations are  
 724 forced at the lower boundary of case 1. The contour intervals are 5 m/s.

725



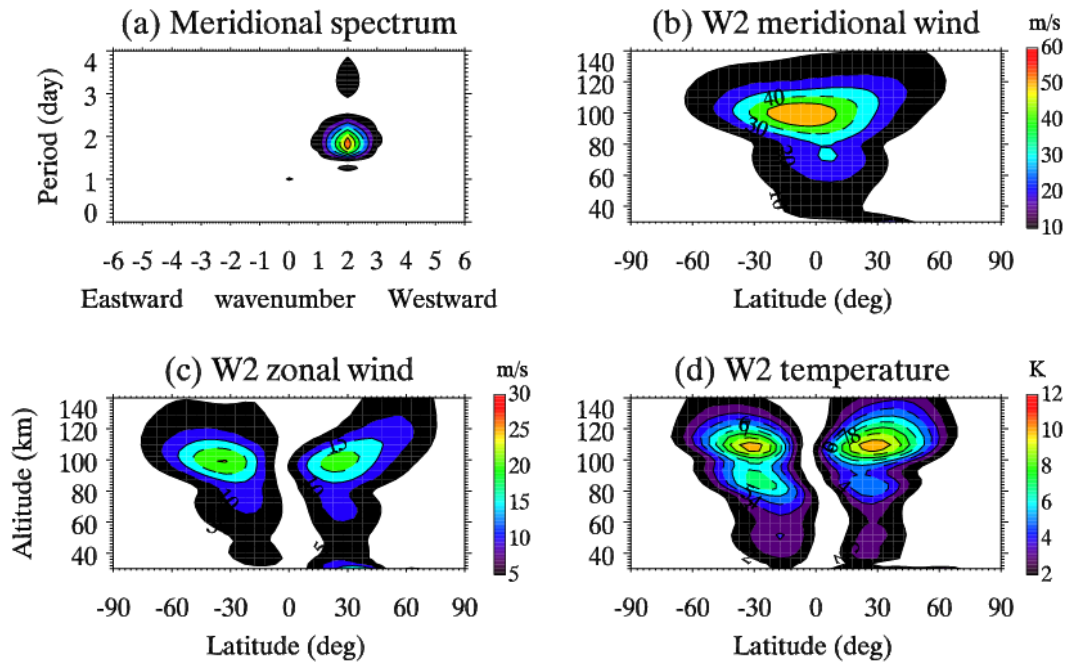
726

727 **Figure 7.** The zonal mean zonal wind during model days 25-30 for (a) case 1, (c) case  
 728 2 and (e) case 3. The baroclinic/barotropic instabilities are overplotted with blue  
 729 shades. The orange shaded region denotes the positive (propagating) waveguide ( $m^2$ )  
 730 for W3. Shown on the right are the EP flux vectors (red arrows) and their divergences  
 731 (light blue shade for positive value, dot line for negative value) for (b) case 1, (d) case  
 732 2 and (f) case 3. The contour intervals for the EP flux divergence are 2 m/s/day.



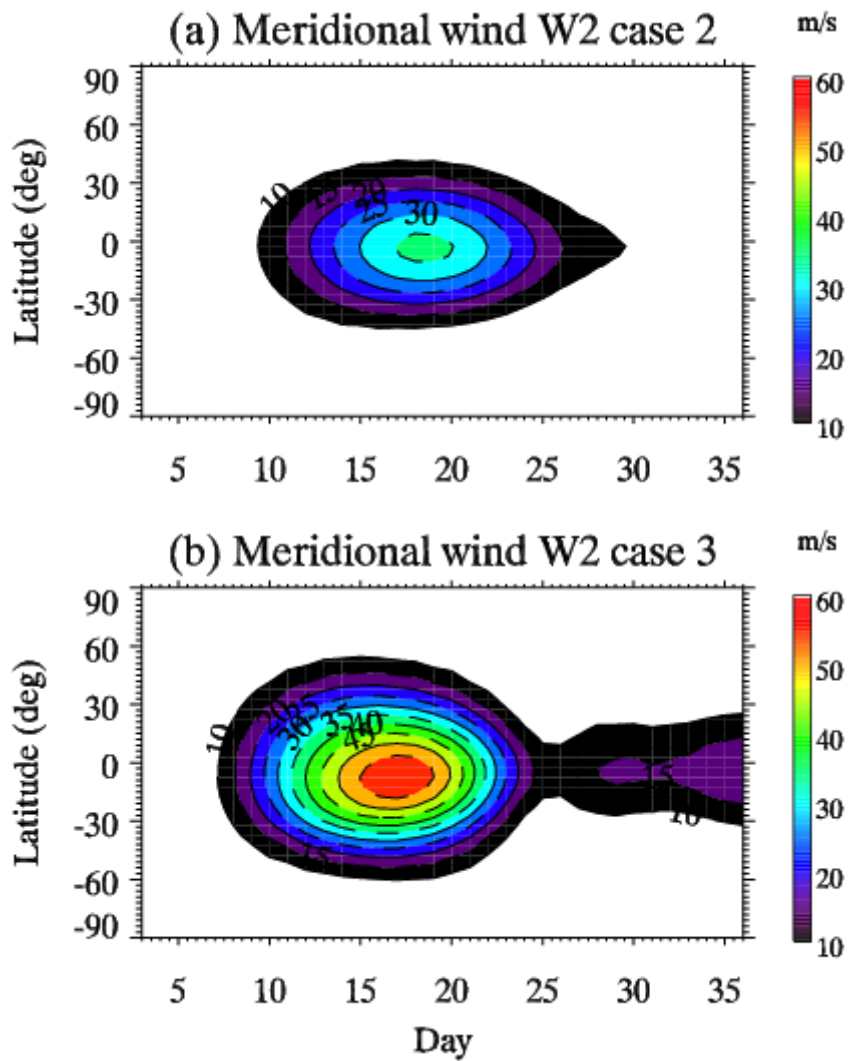
733  
 734  
 735  
 736  
 737

**Figure 8.** (left) Meridional and (right) vertical components of the EP flux of the W3 during model day 25-30 for (a, b) case 1, (c, d) case 2 and (e, f) case 3. The solid contours are for northward or upward directions. Both components have been normalized by the air density.



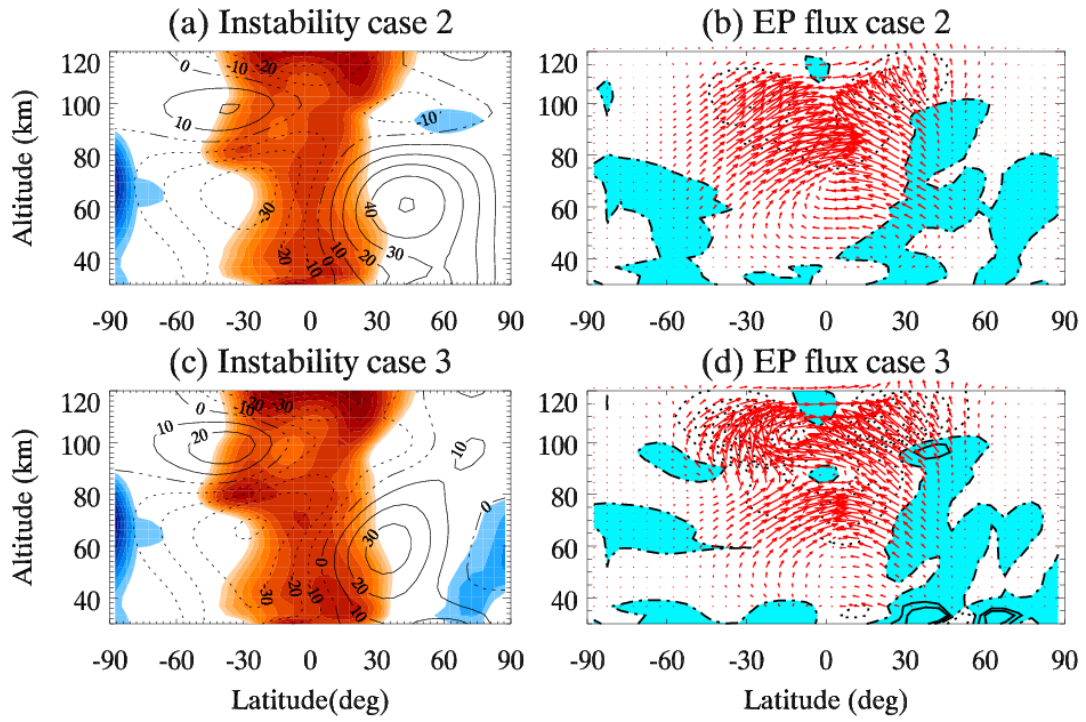
738  
 739  
 740  
 741  
 742

**Figure 9.** Similar to Figure 5 but for case 3 during model days 15-20. Figure 9a shows the meridional wind spectrum at 100 km and 2.5°N. Figures 9b, 9c and 9d show the global and vertical structures of W2 for meridional wind, zonal wind and temperature, respectively.



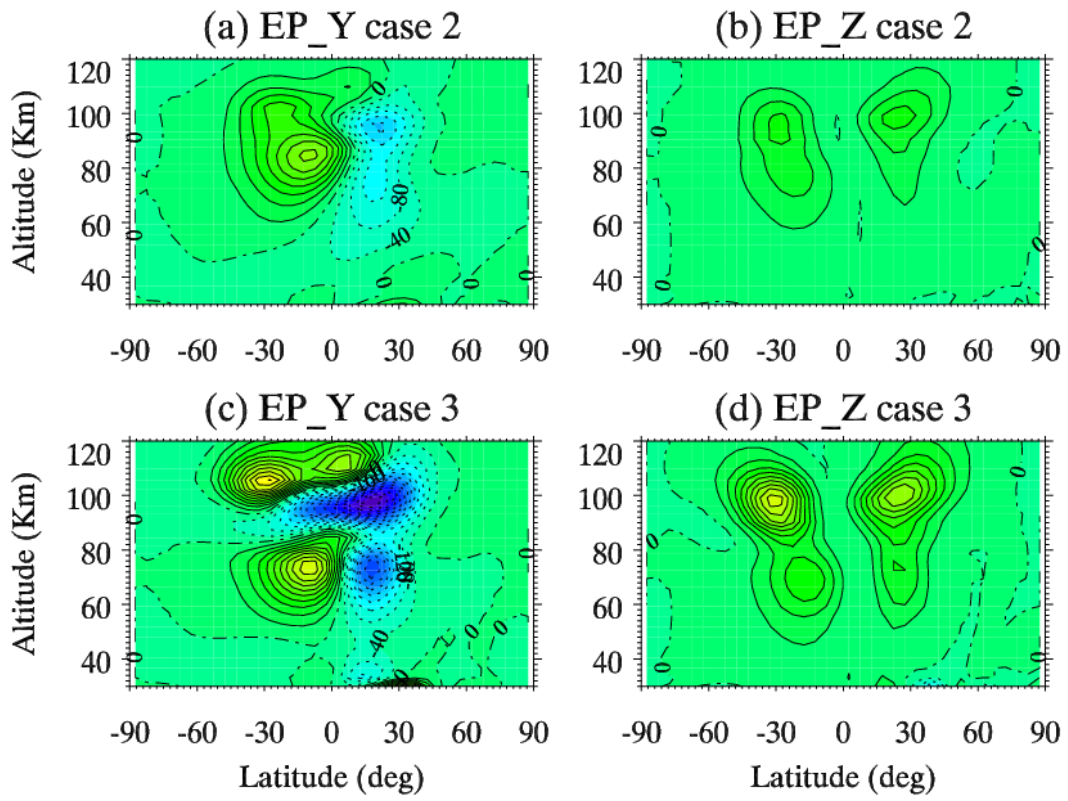
743  
 744  
 745  
 746

**Figure 10.** The temporal variations of the W2 at 100 km for (a) case 2 and (b) case 3. The contour intervals are 5 m/s.



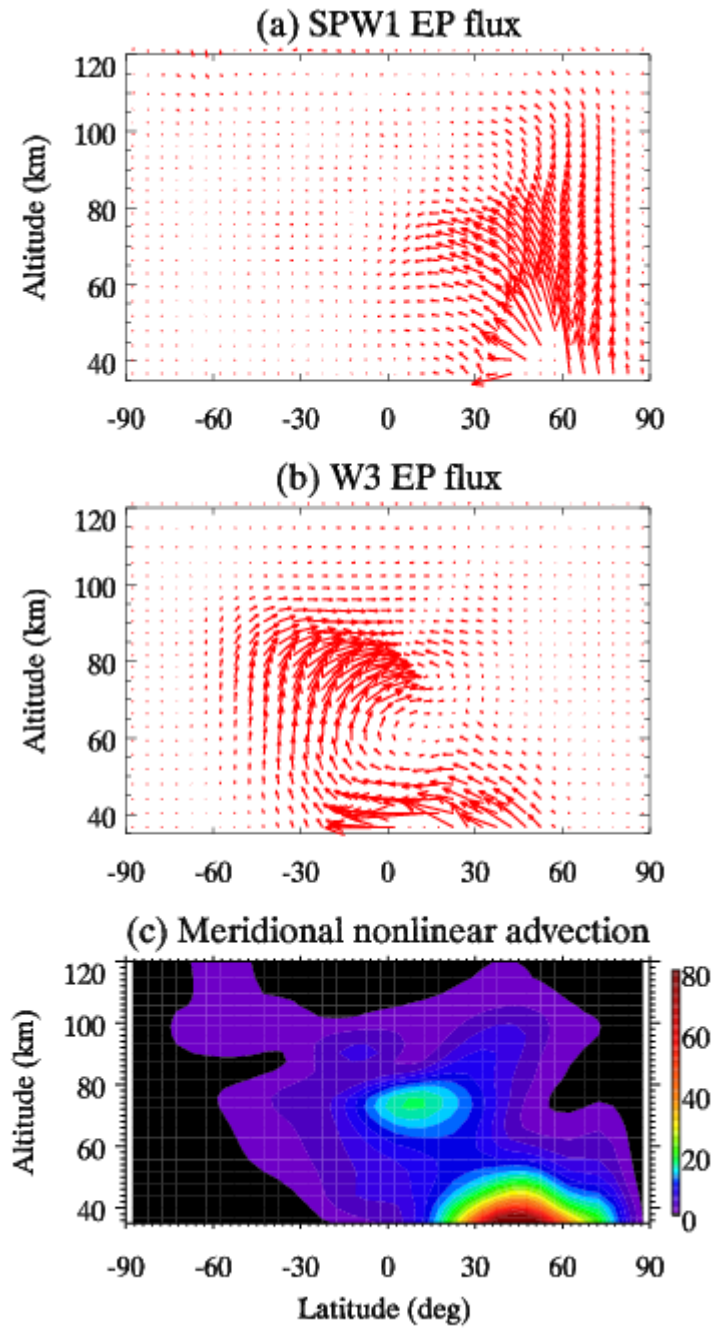
747  
 748  
 749  
 750

**Figure 11.** The same as Figure 7 but for the W2 during model day 15-20 for (a, b) case 2 and (c, d) case 3.



751  
 752  
 753  
 754

**Figure 12.** The same as Figure 8 but for the W2 during model day 15-20 for (a, b) case 2 and (c, d) case 3.



755

756 **Figure 13.** The EP flux vectors of (a) the SPW1 and (b) the W3 during model day

757 15-20 of case 3. (c) The amplitude ( $\text{m/s}^2$ ) of the meridional component of the

758 nonlinear advection tendency between W3 and SPW1.